



Temporal large eddy simulation with lattice Boltzmann methods



Stephan Simonis^{a,b,*}, Daniel Oberle^d, Maximilian Gaedtke^{a,c}, Patrick Jenny^d, Mathias J. Krause^{a,b,c}

^a Lattice Boltzmann Research Group, Karlsruhe Institute of Technology (KIT), 76131 Karlsruhe, Germany

^b Institute for Applied and Numerical Mathematics, Karlsruhe Institute of Technology (KIT), 76131 Karlsruhe, Germany

^c Institute of Mechanical Process Engineering and Mechanics, Karlsruhe Institute of Technology (KIT), 76131 Karlsruhe, Germany

^d Institute of Fluid Dynamics, ETH Zürich, 8092 Zurich, Switzerland

ARTICLE INFO

Article history:

Received 4 December 2020

Received in revised form 4 January 2022

Accepted 14 January 2022

Available online 20 January 2022

Keywords:

Lattice Boltzmann methods

Multiple-relaxation-times

Spectral element method

Temporal large eddy simulation

Direct deconvolution

ABSTRACT

We provide a first investigation of using lattice Boltzmann methods (LBM) for temporal large eddy simulation (TLES). The temporal direct deconvolution model (TDDM) is injected as a closure for the filtered discrete velocity Bhatnagar–Gross–Krook (BGK) Boltzmann equation with orthogonal multiple-relaxation-time (MRT) collision. The novel combination of methods is calibrated for decaying homogeneous isotropic turbulence. The Taylor–Green vortex flow is used as a benchmark for the Reynolds numbers 800 and 3000. Various turbulence quantities are numerically evaluated. The numerical results obtained with the MRT LBM are validated against a well-established spectral element method both, with and without the proposed turbulence model. A qualitatively good agreement to reference results of direct numerical simulation is observed in terms of dissipation rate, energy spectrum and dissipation spectrum. Whereas the latter two show marginal differences compared to underresolved simulations without TLES, the dissipation rate exhibits substantial improvement through the model in capturing the peak region for low and intermediate resolutions. The consistency of the TDDM with first and second order discretization is numerically demonstrated for single-relaxation-time and MRT collision via computing the total dissipation rate error. Measuring the interaction between subgrid activity and energy spectrum error serves as a proof of concept for the proposed MRT LBM TLES. Conclusively, the model recovers and enhances the expected numerical features of LBM with respect to the target equation.

© 2022 Elsevier Inc. All rights reserved.

1. Introduction

As a tool for approximating the incompressible Navier–Stokes equations (NSE) in turbulent flow simulations, the lattice Boltzmann method (LBM) has attracted attention in recent years due to its efficiency and parallelizability [1], especially in connection with large eddy simulation (LES) [2]. The applicability of LBM for direct numerical simulations (DNS) or LES has been investigated in several studies (see for example [3] and references therein). The application of LBM to the LES methodology provides significant speedup over traditional finite volume methods (FVM) [4,5]. In a recent study [6],

* Corresponding author at: Institute for Applied and Numerical Mathematics, Karlsruhe Institute of Technology (KIT), 76131 Karlsruhe, Germany.

E-mail address: stephan.simonis@kit.edu (S. Simonis).

comparing open-source packages for wall-modeled LES of an internal combustion engine demonstrates that LBM (OpenLB [7]) is on average 32 times faster than FVM (OpenFOAM). On an industrial scale in the order of one billion grid cells, LBM LES could even be the first method allowing for overnight simulations [8].

After a first LBM LES model (based on the standard Smagorinsky eddy viscosity) was proposed [9], the approach has been extended [10] to be consistent in the inertial range and complemented with a dynamic procedure [11] for calculating model constants. Weickert et al. [12] proposed and studied an LBM for the wall adaptive large eddy (WALE) model. Based on a Hermite expansion, Malaspina et al. [13] introduced consistent subgrid closures for the filtered Bhatnagar–Gross–Krook (BGK) Boltzmann equation.

Besides LES models based on eddy viscosity approximations, the approximate deconvolution model (ADM) has been formulated in the framework of LBM [14,15] and was extended by adaptive filtering [16,17]. Jacob et al. [18] recently proposed a hybrid approach by combining a recursive regularization technique with hyperviscosity. The simplicity of implementation as well as the vast amount of extension possibilities to other physical flow models promote the necessity of exploring such advanced turbulence models for LBM [15].

Apart from the classical approaches based on spatial filtering, Prueett [19] raised several advantages of time-filtering in the context of LES and introduced a temporal variant of the ADM, called temporal approximate deconvolution model (TADM). Recently a new temporal LES (TLES) based on temporal direct deconvolution (TDDM) was proposed [20]. To the authors' knowledge neither TLES in general nor the TDDM in particular have been combined with LBM before. A TLES upholding the high parallelizability of LBM due to intrinsic spatial locality, along with the benefits of a turbulence model is a promising alternative to classical LES.

Therefore, the purpose of this work is to conduct a primary investigation of utilizing LBM for TLES. In the course of this paper we introduce an MRT LBM TLES based on orthogonal moments [21], dynamic [22] and optimized [23] relaxation frequencies, consistent filtering [13], and temporal direct deconvolution [20]. Its suitability for the numerical simulation of decaying homogeneous isotropic turbulence (DHIT) is evaluated. The Taylor–Green vortex flow is used as a benchmark for the Reynolds numbers 800 and 3000. The novel combination of methods is numerically calibrated via investigating the interaction of the lattice Mach number and the filter width, which are essential to orthogonal MRT LBM and TLES, respectively [24,20]. The capabilities of the present method with respect to turbulence recovery are isolated along the benchmark tests and critically assessed. The results obtained with the present MRT LBM TLES implemented in OpenLB [25,7] are compared to the TDDM [20] implemented in the computational fluid dynamics (CFD) code Nek5000 [26] which is based on spectral element methods (SEM). Moreover, characteristic features of the MRT LBM TLES are quantitatively analyzed via subgrid activity and energy spectrum error measurements [27]. In addition, via computing the total dissipation rate error, the consistency of the TDDM with first and second order discretization is numerically confirmed for single-relaxation-time (SRT) and MRT LBM.

The underlying methodology for the present paper is outlined in Section 2. After recalling the TDDM, as well as the filtered equation levels within the derivation of LBM, the MRT LBM TLES is assembled. Subsequently, the novel method is calibrated for DHIT, compared to the SEM TLES with respect to DNS results, and numerically evaluated in Section 3. Section 4 closes the paper and suggests further studies. Methodological modifications and numerical consistency results are provided in Appendices A and B, respectively.

2. Methodology

2.1. Temporal large eddy simulation

The TDDM [20] is based on an Eulerian time domain filtering for a time dependent function g , i.e.

$$\bar{g}(t; \Theta) = \int_{-\infty}^t G(t' - t; \Theta) g(t') dt', \quad (1)$$

where G is the filter kernel, and the scalar $\Theta > 0$ specifies the filter width. Temporally filtering the incompressible NSE results in

$$\frac{\partial \bar{u}_\alpha}{\partial x_\alpha} = 0, \quad (2)$$

$$\frac{\partial \bar{u}_\alpha}{\partial t} + \frac{\partial \bar{u}_\alpha \bar{u}_\beta}{\partial x_\beta} = -\frac{1}{\rho} \frac{\partial \bar{p}}{\partial x_\alpha} + \nu \frac{\partial^2 \bar{u}_\alpha}{\partial x_\beta \partial x_\beta} - \frac{\partial T_{\alpha\beta}}{\partial x_\beta}, \quad (3)$$

where \bar{u} and \bar{p} are the filtered velocity and pressure, respectively. By using the exponential function as filter kernel, the differential form of the filter operator can be written as

$$\frac{\partial}{\partial t} \bar{\Upsilon} = \frac{\Upsilon - \bar{\Upsilon}}{\Theta}, \quad (4)$$

where $\Upsilon \in \{\mathbf{u}, p\}$ is an unfiltered quantity. The filtering operation is reversed by rearranging (4) to

$$\Upsilon = \bar{\Upsilon} + \Theta \frac{\partial \bar{\Upsilon}}{\partial t}. \quad (5)$$

This process is referred to as direct deconvolution [20]. Applying the same procedure to the convective term $\bar{u}_\alpha \bar{u}_\beta$, an ordinary differential equation which describes the time evolution of the temporal residual stress tensor $T_{\alpha\beta} = \bar{u}_\alpha \bar{u}_\beta - \bar{u}_\alpha \bar{u}_\beta$ can be obtained, hence

$$\frac{\partial T_{\alpha\beta}}{\partial t} = -\frac{T_{\alpha\beta}}{\Theta} + \Theta \frac{\partial \bar{u}_\alpha}{\partial t} \frac{\partial \bar{u}_\beta}{\partial t}. \quad (6)$$

Together with the trivially filtered solenoidal condition (2), equations (3) and (6) form a closed system.

2.2. Filtered BGK Boltzmann equation

The filtered Boltzmann equation (FBE) with the BGK collision operator as derived by Malaspinas et al. [13] reads

$$\frac{\partial \bar{f}}{\partial t} + (\xi \cdot \nabla) \bar{f} = -\frac{1}{\tau} [\bar{f} - f^{\text{eq}}(\bar{f})] + \frac{1}{\tau} \mathcal{R}, \quad (7)$$

where $\bar{f} : \Omega \times \Xi \times I \rightarrow \mathbb{R}$, $(\mathbf{x}, \xi, t) \mapsto \bar{f}(\mathbf{x}, \xi, t)$ is the filtered particle distribution function dependent on space $\mathbf{x} \in \Omega$, velocity $\xi \in \Xi$ and time $t \in I$. Further, $\mathcal{R} = [\bar{f}^{\text{eq}} - f^{\text{eq}}(\bar{f})]$ defines the residual and τ denotes the relaxation time. The injection of a Hermite expansion for the equilibrium distribution function f^{eq} into \mathcal{R} , i.e.

$$\mathcal{R} = w(\xi) \sum_{n=0}^N \mathcal{H}^{(n)}(\xi) : \mathcal{R}^{(n)}, \quad (8)$$

where $\mathcal{H}^{(n)}$ denotes the n -th order multi-dimensional Hermite polynomial, allows an order by order expression [13]. Hence, up to second order ($N = 2$) we obtain

$$\mathcal{R}^{(0)} = 0, \quad (9)$$

$$\mathcal{R}_\alpha^{(1)} = 0, \quad (10)$$

$$\mathcal{R}_{\alpha\beta}^{(2)} = T_{\alpha\beta} + \eta \delta_{\alpha\beta}, \quad (11)$$

where T and η are subgrid stress and subgrid temperature, respectively. Since the incompressible NSE is chosen as target equation (TEQ), we aim at an isothermal second order truncation, such that the subgrid temperature simplifies to $\eta \equiv 0$. For the remainder term $\mathcal{R}_{\alpha\beta}^{(2)}$ usually an eddy viscosity model is used to approximate the distinct tensorial orders. Here we take a different route, interpret T in the context of TLES as the temporal residual stress tensor, and outsource (6) as follows.

2.3. Time-filtered discrete velocity BGK Boltzmann equation

With (9), the Hermite series truncation at order two, and the use of a D3Q19 velocity stencil, (7) forms the filtered discrete velocity BGK Boltzmann equation (FDVBE)

$$\frac{\partial \bar{f}_i}{\partial t} + (\xi_i \cdot \nabla) \bar{f}_i = -\frac{1}{\tau} [\bar{f}_i - f_i^{\text{eq}}(\bar{f})] + \underbrace{\frac{1}{\tau} \frac{1}{2c_s^4} w_i \mathcal{H}_{i\alpha\beta}^{(2)} T_{\alpha\beta}}_{=: R_i}, \quad (12)$$

where $\mathcal{H}_i^{(2)}$ denotes the second order multi-dimensional Hermite polynomial in ξ_i for $i = 0, 1, \dots, q-1$. The discrete velocity equilibrium resulting from the truncation is given by

$$f_i^{\text{eq}}(\bar{f}) = w_i \bar{\rho} \left(1 + \frac{1}{c_s^2} \xi_{i\alpha} \bar{u}_\alpha + \frac{1}{2c_s^4} \mathcal{H}_{i\alpha\beta}^{(2)} \bar{u}_\alpha \bar{u}_\beta \right), \quad (13)$$

where w_i specifies the classical weights for D3Q19, and c_s denotes the corresponding lattice speed of sound. Note that the dependence of f_i^{eq} on \bar{f} is given by the typical zeroth and first order moment summation for recovering the hydrodynamic conservative variables $\bar{\rho}$ and $\bar{\mathbf{u}}$ [13]. Hence, we can form a closed system of equations, consisting of (6), (12), and (13).

2.4. Time-filtered lattice Boltzmann equation

Finally, a lattice Boltzmann evolution rule is obtained by complete discretization on a Cartesian grid $(\mathbf{x}, t) \in \Omega_{\Delta x} \times I_{\Delta t}$. Classical second order discretization [13,28] of (12) leads to the filtered lattice Boltzmann equation (FLBE)

$$n_i(\mathbf{x} + \Delta t \xi_i, t + \Delta t) = n_i(\mathbf{x}, t) - \frac{\Delta t}{\tau + \frac{\Delta t}{2}} \{ [n_i(\mathbf{x}, t) - f_i^{\text{eq}}(\mathbf{n})] + R_i(\mathbf{x}, t) \} \quad (14)$$

where \mathbf{n} is the filtered and implicitly shifted version of \mathbf{f} . Hence, with the standard zeroth and first order moment summation leading to $\bar{\rho}$ and $\bar{\mathbf{u}}$, respectively, we expect convergence with second order in space and first order in time under diffusive scaling (DS) [1,13] towards (2) and (3) with a viscosity recovered by

$$\nu = c_s^2 \left(\tau - \frac{\Delta t}{2} \right). \quad (15)$$

Further implications on scaling laws and the corresponding experimental order of convergence are provided in Appendix B. To attribute the method with stabilization features [22] we introduce a multiple-relaxation-time (MRT) collision in moment space [21]. In matrix-vector form, the MRT FLBE then reads

$$\mathbf{n}(\mathbf{x} + \Delta t \xi_i, t + \Delta t) = \mathbf{n}(\mathbf{x}, t) - \Delta t K \{ [\mathbf{n}(\mathbf{x}, t) - \mathbf{f}^{\text{eq}}(\mathbf{n})] + \mathbf{R}(\mathbf{x}, t) \}, \quad (16)$$

where

$$\mathbf{R}(\mathbf{x}, t) = \frac{1}{2c_s^4} \left(w_i \mathcal{H}_{i\alpha\beta}^{(2)} T_{\alpha\beta}(\mathbf{x}, t) \right)_{i=0,1,\dots,q-1}^T. \quad (17)$$

Whereas the orthogonal moment basis M , which in turn is manifested within the collision matrix $K = M^{-1}SM \in \text{GL}_q(\mathbb{R})$, is defined as in [21], the equilibrium moments are consistent to SRT formulations (i.e. in terms of the notation of [21]: $w_\epsilon = 3$, $w_{\epsilon j} = 17/2$, $w_{xx} = 2$). Hence, by construction, the present MRT collision is consistent to the derivation for SRT above. In this regard, we remark that the present definition of \mathbf{R} is *unrelaxed* in contrast to [13, Equation (4.46)]. The relaxation matrix S comprises the hydrodynamic relaxation rates suggested in [21], and the optimized values of the kinetic relaxation frequencies proposed in [23]. Motivated by linear and brute force analysis [22], the latter are used here to obtain dynamic relaxation functions with respect to the lattice Mach number Ma which are further specified in Section 3.2.2.

To compute the remainder term, the forward Euler method with forward differenced time derivatives of $\bar{\mathbf{u}}$ is used for the discretization of (6), i.e.

$$T_{\alpha\beta}(\mathbf{x}, t) = \left(1 - \frac{\Delta t}{\Theta} \right) T_{\alpha\beta}(\mathbf{x}, t - \Delta t) + \frac{\Theta}{\Delta t} \{ [\bar{u}_\alpha(\mathbf{x}, t) - \bar{u}_\alpha(\mathbf{x}, t - \Delta t)][\bar{u}_\beta(\mathbf{x}, t) - \bar{u}_\beta(\mathbf{x}, t - \Delta t)] \}. \quad (18)$$

Discrete unfiltered variables can be recovered via backward differencing the deconvolution rule (5), namely

$$\Upsilon(\mathbf{x}, t) = \bar{\Upsilon}(\mathbf{x}, t) + \frac{\Theta}{\Delta t} [\bar{\Upsilon}(\mathbf{x}, t) - \bar{\Upsilon}(\mathbf{x}, t - \Delta t)]. \quad (19)$$

It is notable that both (18) and (19) are local in space. Implementation-wise, increasing the discretization order requires additional memory storage. For the sake of completeness, a second order discretization of the here used TDDM is presented in Appendix A and tested in Appendix B for both SRT and MRT collision.

3. Numerical tests

This section summarizes the results obtained from conducting benchmark tests for DHIT to evaluate the quality of the method with respect to DNS results with SEM. If not stated otherwise, we assume a physical SI unit system and neglect its consistent notation from now on.

3.1. Taylor–Green vortex flow

Let the domain comprise a fully periodic cube $\Omega = [0, 2\pi l_c]^3$. Characteristic scales are denoted as l_c , U_c and ρ_c . With $l_c = 1\text{m}$, $U_c = 1\text{m/s}$, the Reynolds number can be defined as $Re = (1 \text{ m}^2/\text{s})/\nu$. The initial velocity field for the Taylor–Green vortex (TGV) flow [29,24] reads

$$\mathbf{u}(\mathbf{x}, 0) = \begin{pmatrix} U_c \sin\left(\frac{x}{l_c}\right) \cos\left(\frac{y}{l_c}\right) \cos\left(\frac{z}{l_c}\right) \\ -U_c \cos\left(\frac{x}{l_c}\right) \sin\left(\frac{y}{l_c}\right) \cos\left(\frac{z}{l_c}\right) \\ 0 \end{pmatrix}. \quad (20)$$

Further, the initial pressure is set to

$$p(\mathbf{x}, 0) = p_\infty + \frac{\rho_c U_c^2}{16} \left[\cos\left(\frac{2x}{l_c}\right) + \cos\left(\frac{2y}{l_c}\right) \right] \left[\cos\left(\frac{2z}{l_c}\right) + 2 \right], \quad (21)$$

where p_∞ labels a reference pressure.

3.1.1. Turbulence quantities

To evaluate the simulation quality, the following turbulence quantities are computed. Via the kinetic energy [30]

$$k(t) = \frac{1}{|\Omega|} \int_{\Omega} \frac{1}{2} \mathbf{u}^2 d\mathbf{x} \quad (22)$$

and the enstrophy [30]

$$\zeta(t) = \frac{1}{|\Omega|} \int_{\Omega} (\nabla \times \mathbf{u})^2 d\mathbf{x}, \quad (23)$$

the total dissipation rate

$$\epsilon_{\text{tot}}(t) = -\frac{dk}{dt} \quad (24)$$

and the resolved (enstrophy-based) dissipation rate [31]

$$\epsilon_{\text{res}}(t) = 2\pi\nu\zeta \quad (25)$$

are extracted. Subtraction leads to the model dissipation rate

$$\epsilon_{\text{mod}} = \epsilon_{\text{tot}} - \epsilon_{\text{res}}, \quad (26)$$

which quantifies the artificial residual portion of ϵ_{tot} injected by the model [32]. Further, we measure the instantaneous directionally stripped energy spectrum $E(\kappa, t)$ [33,34] and with it, the dissipation spectrum

$$D(\kappa, t) = 2\nu\kappa E(\kappa, t), \quad (27)$$

where κ denotes the wavenumber.

3.1.2. Reference data

In the following, a high resolution DNS with the SEM, resolving the appearing scales, serves as a reference. The simulations denoted with SEM were performed using the spectral element code Nek5000 [26]. The solver employs third order backward differentiation formulas in time and a spatial discretization which depends on the chosen polynomial order [35].

Two Reynolds numbers are tested, $Re = 800$ and $Re = 3000$, respectively. The discretization for the former is based on 18 spectral elements in each coordinate direction with a polynomial order of seven, which equals a number of $N = 127$ grid points. For the second tested Reynolds number $Re = 3000$, the resolution of the reference SEM DNS is $N = 351$ in each coordinate direction, consisting of 50 elements and a polynomial order of seven. Both reference simulations use a timestep size of $\Delta t = 0.001$.

Fig. 1 exemplarily visualizes the time-dependent spectra of energy and dissipation for $Re = 800$ computed with SEM DNS. The sampling rate of the kinetic energy is 0.05. The time dependence of the TGV flow in terms of spectral properties is clearly evident. It is also notable that, due to the low Reynolds number, the majority of dissipation takes place within the low to intermediate wavenumber region (see Fig. 1b).

3.2. Model calibration

To scrutinize the numerical behavior of the TLES LBM proposed above, a parameter study is conducted. The observed effects of the temporal filter for varying lattice Mach number and filter width are categorized below. Therefor, ϵ_{tot} , ϵ_{res} , ϵ_{mod} , E , and D are evaluated for a Reynolds number of $Re = 800$. If not stated otherwise, all quantities are deconvolved according to (19). For clarity, Table 1 summarizes the typical conversion factors for LBM including some of parameter choices used in the present work. All LBM computations are carried out with OpenLB [7,25] on at most 75 nodes with two Intel Xeon E5-2660 v3 each.

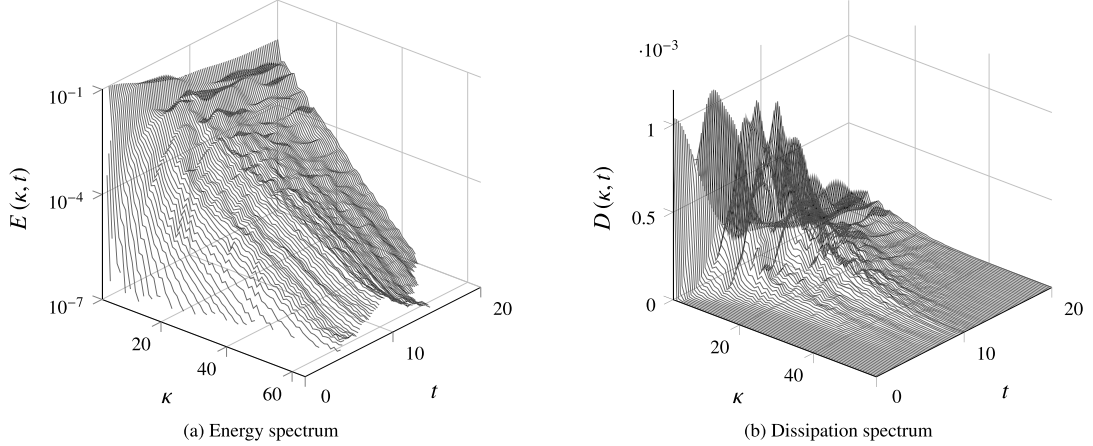


Fig. 1. DNS results of the TGV flow computed with the SEM ($N = 127$, $Re = 800$). Energy spectrum $E(\kappa, t)$ and dissipation spectrum $D(\kappa, t)$ plotted over time t and wavenumber κ .

Table 1
Summary of LBM discretization parameters.

N	u^L	Ma	Δx	Δt	τ	
					$Re = 800$	$Re = 3000$
64	0.11547	0.2	0.09973	0.01154	0.50434	0.50116
	0.08660	0.15	0.09973	0.00864	0.50326	0.50087
	0.05776	0.1	0.09973	0.00576	0.50217	0.50058
	0.04330	0.075	0.09973	0.00432	0.50163	0.50043
	0.02887	0.05	0.09973	0.00288	0.50109	0.50029
128	0.11547	0.2	0.04947	0.00571	0.50875	0.50233
	0.08660	0.15	0.04947	0.00428	0.50656	0.50175
	0.05776	0.1	0.04947	0.00288	0.50438	0.50117
	0.04330	0.075	0.04947	0.00214	0.50328	0.50088
	0.02887	0.05	0.04947	0.00144	0.50219	0.50058

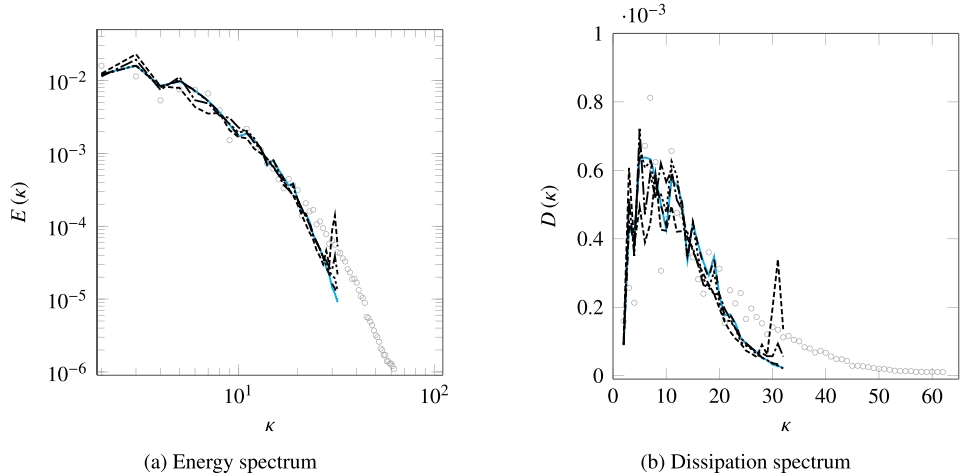


Fig. 2. Energy spectrum $E(\kappa)$ (a) and dissipation spectrum $D(\kappa)$ (b) at $t = 9$ for the TGV flow with $Re = 800$. Computations for $Ma = 0.1$ and $N = 64$ with LBM as UDNS and TLES with $\tilde{\Theta} = 5, 10, 20, 40$ in comparison to the SEM DNS with a corresponding resolution of $N = 127$.

3.2.1. Filter width

Let

$$\Theta = \tilde{\Theta} \Delta t, \quad (28)$$

where $\tilde{\Theta} > 0$ denotes the dimensionless filter width. To calibrate the model, we test a sequence of $\tilde{\Theta} = 5, 10, 20, 40$ for the MRT LBM TLES with a fixed Mach number of $Ma = 0.1$ and a resolution of $N = 64$ for the TGV flow with $Re = 800$.

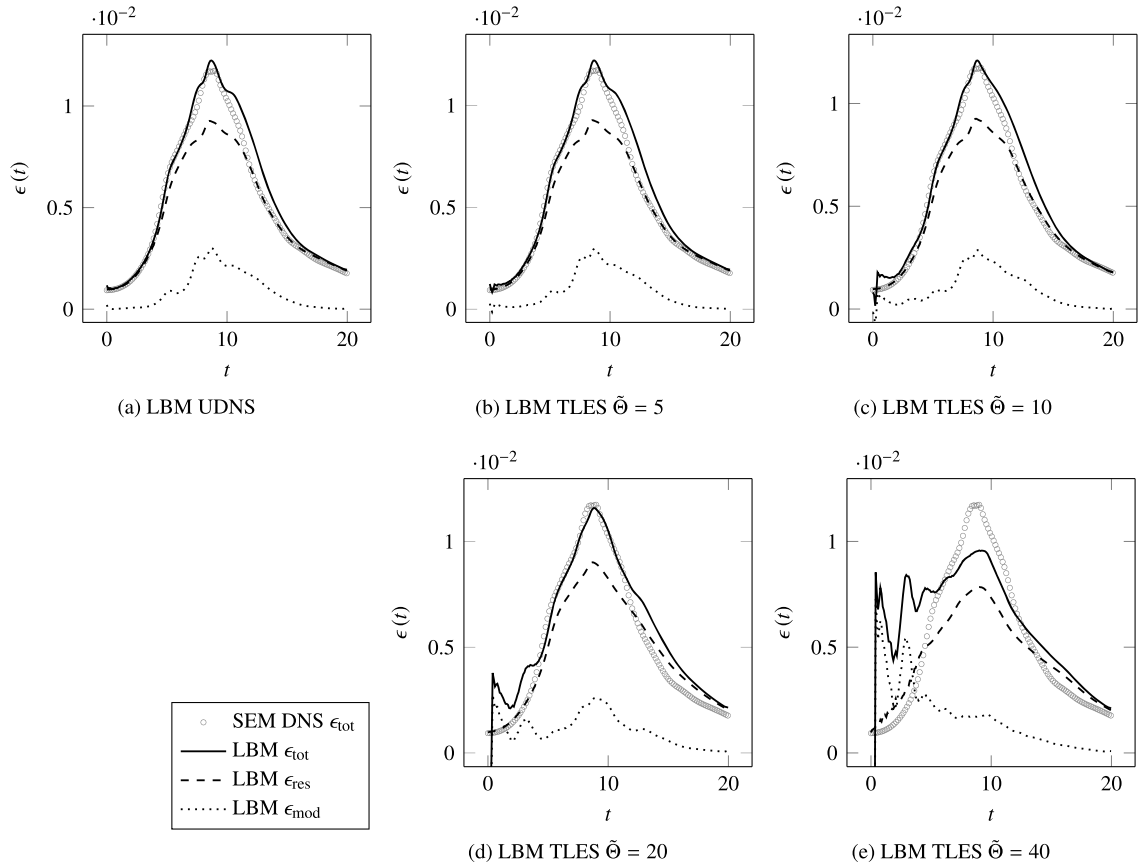


Fig. 3. Total, resolved and model dissipation rate for the TGV flow with $Re = 800$. Computations for $Ma = 0.1$ and $N = 64$ with LBM as UDNS (a) and TLES with $\tilde{\Theta} = 5, 10, 20, 40$ (b-e, respectively) in comparison to the SEM DNS with a corresponding resolution of $N = 127$.

The resulting effects on dissipative properties and spectral energy recovery are plotted in Figs. 3 and 2, respectively. For $\tilde{\Theta} = 5$ the impact of the TLES on the dissipation rate is marginally visible when comparing Figs. 3a and 3b. Also the spectral properties of UDNS and TLES are similar for the smallest investigated filter width. Nevertheless, a slight increase of ϵ_{mod} shortly after the initialization is evident. In case of $\tilde{\Theta} = 10, 20$, the peak of ϵ_{tot} approaches the reference DNS solution, see Figs. 3c and 3d. At the same time, the model dissipation rate oscillations in the initial time zone accumulate until a complete overdrive, which proceeds with time, is visible for $\tilde{\Theta} = 40$ (Fig. 3e). Conclusively it can be stated that for $\tilde{\Theta} > 10$ the dissipation rate oscillations are clearly unphysical. The effects also project to wavenumber space, where a respective increase within the energy (Fig. 2a) as well as the dissipation spectrum (Fig. 2b) appears at high wavenumbers $\kappa \gtrsim 30$. Further, Fig. 2 suggests that for $\tilde{\Theta} \rightarrow 40$ the model draws energy from the inertial range and transports it to small scales. Hence, increasing the filter width leads to a larger amount of energy injection into the dissipation range.

Conclusively, since the spectra remain close to the UDNS, initial oscillations are kept in a reasonable intensity and the dissipation rate peak is a closer match than without the model, the filter width is set to $\tilde{\Theta} = 10$ for all following LBM TLES runs.

3.2.2. Lattice Mach number dependency

We test the method for a range of $Ma = 0.05, 0.075, 0.1, 0.15, 0.2$ to investigate the dependency on the timestep size which changes along the Mach number variation. Due to the fact that MRT LBM exhibits lattice Mach number instabilities [24,36], the free parameters of the MRT are modified to obtain stable results. The optimized third order relaxation frequencies proposed by Chávez-Modena et al. [23] are Ma -dependent [22]. To respect this dependency, a polynomial fit is used in the present work, assigning the corresponding value for each of the tested Ma to the third order relaxation frequencies. Overall, the here used relaxation frequencies can be summarized in the non-dimensional notation of [22] to second order $s_e = 1.19$ (static) and $s_p = 2c_s^2/(2\nu + c_s^2)$ (shear viscosity conforming to (15)), third order $s_q(Ma) = 35Ma^3 - 26.5Ma^2 + 8.5Ma$ and $s_\mu(Ma) = (200/3)Ma^3 - 45Ma^2 + (71/6)Ma$ (dynamic relaxation functions), and fourth order $s_e = s_{\Pi} = 1.4$ (static). A detailed stability analysis of the such obtained model is given in [22].

Fig. 5 summarizes the dissipation rate changes along the variation of Ma . Spectral energy and dissipation are visualized in Fig. 4. Tracking the previous observations for the filter width variation, we detect an amplification of the dissipation rate

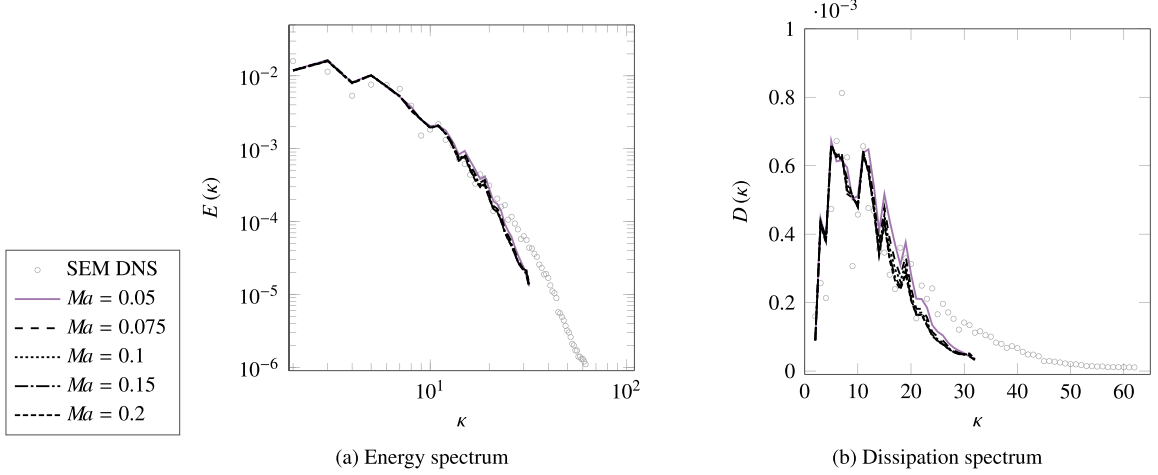


Fig. 4. Energy spectrum $E(\kappa)$ (a) and dissipation spectrum $D(\kappa)$ (b) at $t = 9$ for the TGV flow with $Re = 800$. Computations for $N = 64$ with LBM TLES ($\tilde{\Theta} = 10$) for $Ma = 0.05, 0.075, 0.1, 0.15, 0.2$ in comparison to the SEM DNS with a corresponding resolution of $N = 127$.

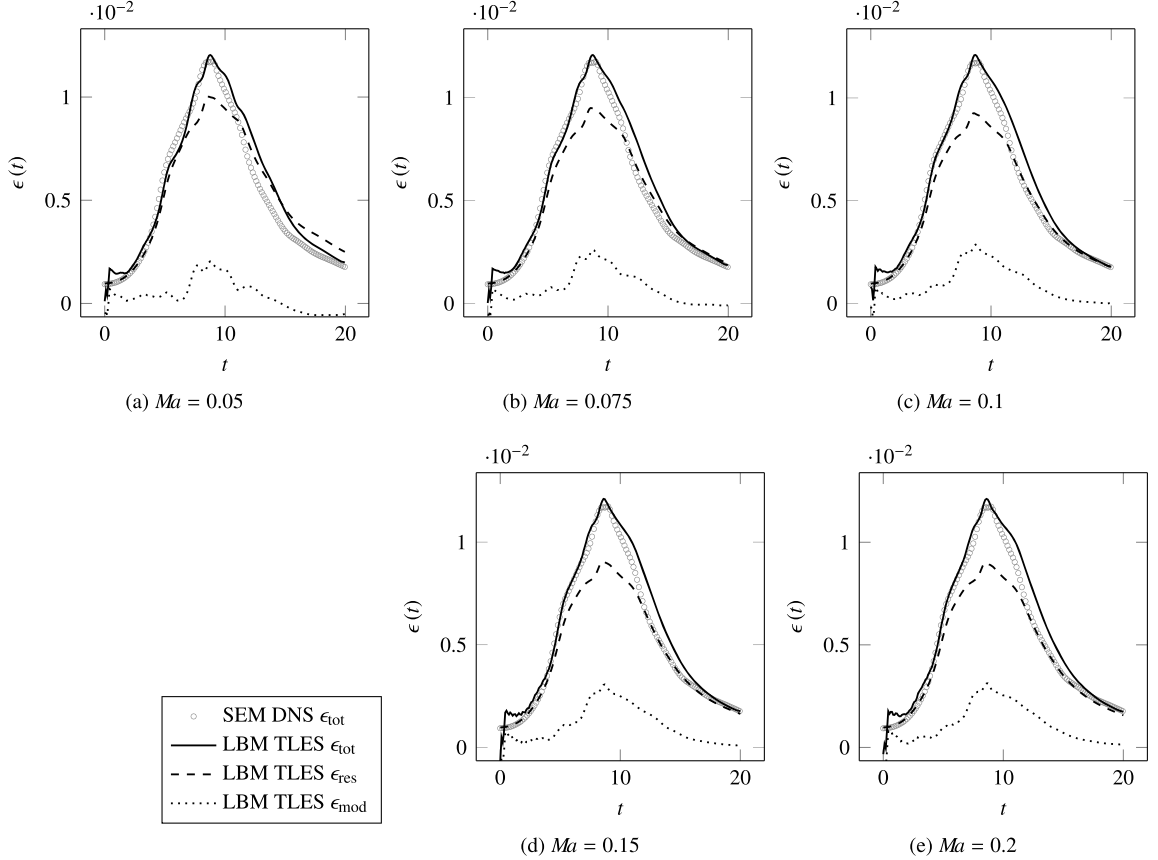


Fig. 5. Total, resolved and model dissipation rate for the TGV flow with $Re = 800$. Computations for $N = 64$ with LBM TLES ($\tilde{\Theta} = 10$) for $Ma = 0.05, 0.075, 0.1, 0.15, 0.2$ (a-e, respectively) in comparison to the SEM DNS with a corresponding resolution of $N = 127$.

oscillations at $t \rightarrow 0$ with increasing Ma (see e.g. Fig. 5d). Though a similar effect of analogously increasing energy and dissipation in high wavenumbers is shown in Fig. 4, the spectral quantities are less affected by varying Ma .

In contrast to the unphysical oscillations for increasing Ma , the lowest evaluated Mach number causes clearly negative model dissipation. This behavior roots in the model's compensation of an unphysically increased resolved dissipation rate for $t > 10$ (see Fig. 5a). The fact that the model is applied to TGV flow, where the effective Mach number decreases with time

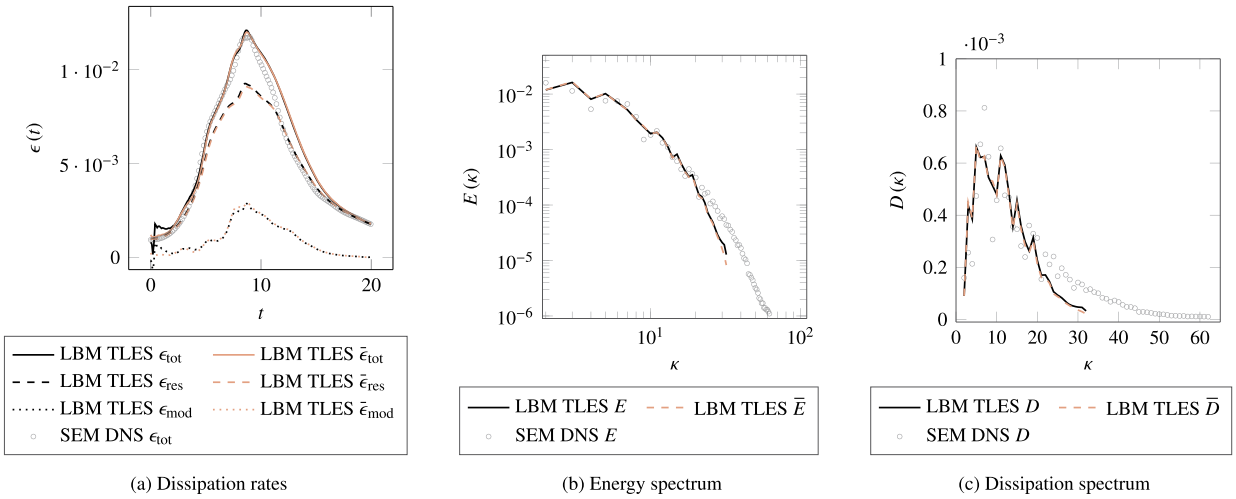


Fig. 6. Dissipation rates $\epsilon_{\text{tot}}(t)$, $\epsilon_{\text{res}}(t)$, $\epsilon_{\text{mod}}(t)$ (a), energy spectrum $E(\kappa)$ (b) and dissipation spectrum $D(\kappa)$ (c) (at $t = 9$) for the TGV flow with $Re = 800$. Computations for $N = 64$ with LBM TLES ($\Theta = 10$) for $Ma = 0.1$. Deconvolved and filtered quantities in comparison to the SEM DNS with a corresponding resolution of $N = 127$.

underlines the statement. Our observations confirm that the computation up to $t = 20$ is essential for the critical evaluation of the solver. The lowest tested Mach number which does not exhibit an overly increased dissipation rate tail is $Ma = 0.1$. Another argument for choosing Ma rather smaller than the usually “incompressible enough” value of 0.3 is constituted by the fact that we obtained an expression for the residual stress T from the filtered *incompressible* NSE in the first place. Contrary to this, LBM approximates the weakly compressible NSE [13], solely reaching the incompressible limit under DS [1], i.e. diminishing the Mach number via $\Delta t = \mathcal{O}(\Delta x^2)$ along $\Delta x \rightarrow 0$.

As a compromise between computational effort, which increases when decreasing the Mach number, and the circumstances addressed above, we fix $Ma = 0.1$ for the following simulations.

3.2.3. Deconvolution of filtered quantities

Fig. 6 gives an overview of all computed quantities in filtered and deconvolved form. With respect to the observations above, it becomes clear that the initial dissipation rate deviation in Fig. 6a roots in the LBM itself and is amplified by the turbulence model. In particular, despite initializing the velocity field, pressure and strain rate with respective populations, the intrinsic feature of LBM applied to a nonstationary TEQ—transporting initialization errors with time throughout the whole simulation—remains present. Consequently, the first order finite differences in the evolution equation for T (18) as well as in the discrete deconvolution (19) act as amplifiers for initialization errors of LBM. The intensifying initial time oscillations with increased Mach numbers are also in line with this argument. A larger Ma increases Δt as well as the compressibility error, and consequently the initialization error [37]. In turn, larger filter widths amplify that error and lead to higher deviation at early timesteps.

Except for the initial dissipation rate oscillations and the corresponding spectra deviations at the highest wavenumbers $\kappa \approx 30$, only marginal differences are observable in Fig. 6. Within the remaining region of resolved wavenumbers, the deconvolved and filtered spectra of energy (Fig. 6b) and dissipation (Fig. 6c), respectively, are overall in close agreement.

3.3. Comparison to the spectral element method

The Reynolds number is increased to $Re = 3000$ to reach the turbulent regime which shifts the dissipation spectrum to higher wavenumbers. The optimal parameters for the LBM TLES with respect to above investigations where set to $\Theta = 10$ and $Ma = 0.1$.

A comparison to the recently proposed SEM TLES [20] is conducted. The only modification compared to the implementation in [20] is the regularization term. As expected, relaxing the unfiltered velocity fields to the filtered ones within the regularization, introduces a phase lag. Although its effect is negligible in statistically stationary test cases, it proved to be severe for the results of the TGV flow due to its transient nature. This effect can be prevented by using the regularization term from the TADM [19]. In this term, the filtered fields are relaxed to their filtered approximate deconvolution.

To find common ground for both methods, the respective number of elements was chosen such that the overall resolution of the SEM closely matches the number of Cartesian gridpoints of the LBM. The resolution $N = 64$ of the UDNS and the TLES with SEM consists of nine spectral elements in each coordinate direction and a polynomial order of seven. The parameters used for the SEM TLES comprise the filter width $\Theta = 10\Delta t$ and the regularization parameter $\chi = 4.0$, with a timestep size of $\Delta t = 0.005$. In contrast to that, the resolution $N = 127$ of the UDNS and TLES with SEM consists of 18 spectral elements in each coordinate direction and a polynomial order of seven. The parameter choices for the SEM TLES in this case are

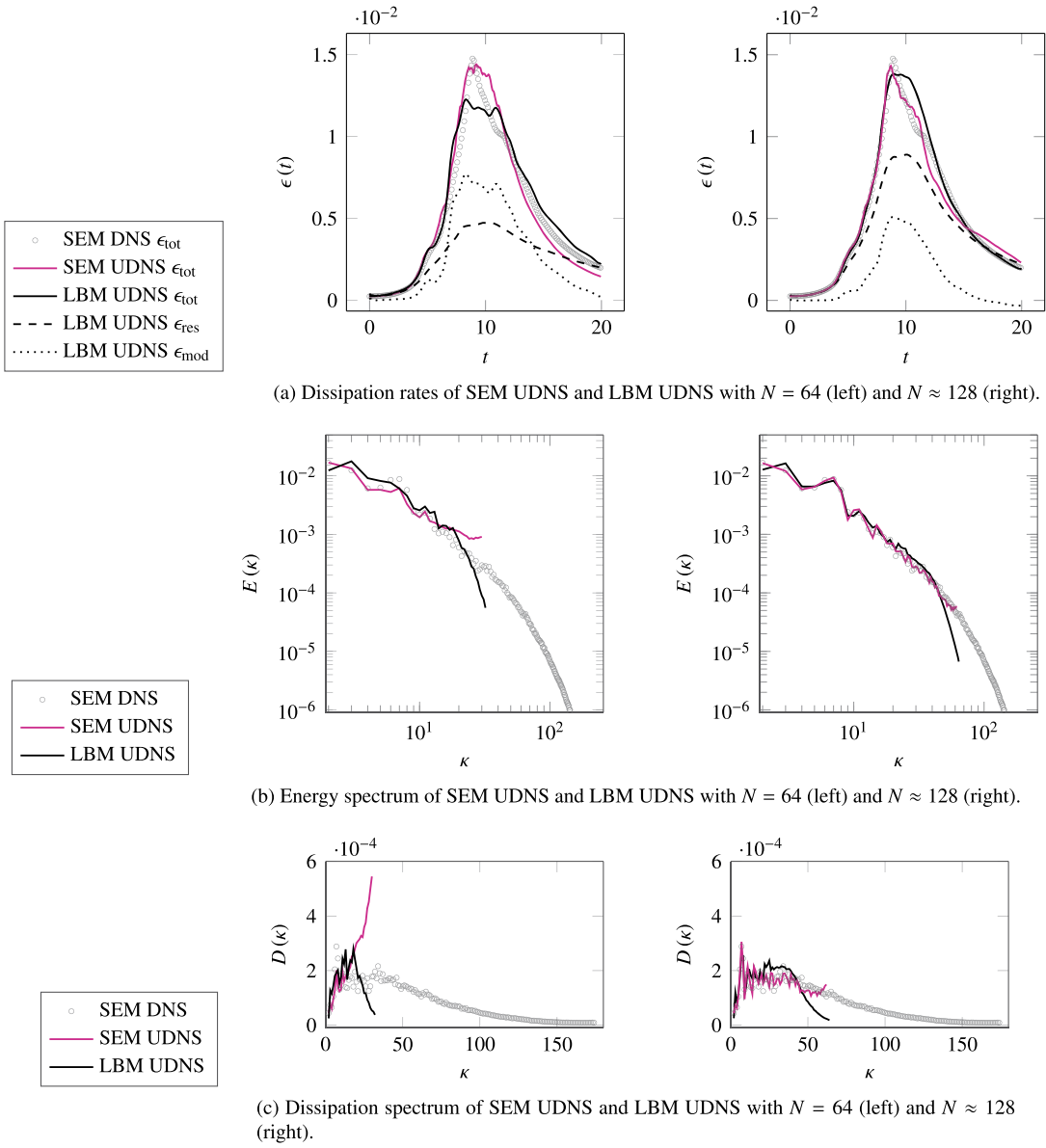


Fig. 7. Dissipation rates $\epsilon_{\text{tot}}(t)$, $\epsilon_{\text{res}}(t)$, $\epsilon_{\text{mod}}(t)$, energy spectrum $E(\kappa)$ and dissipation spectrum $D(\kappa)$ (at $t = 9$) for the TGV flow with $Re = 3000$. Computations for $N = 64$ (left column) and $N \approx 128$ (right column) with LBM UDNS for $Ma = 0.1$ compared to SEM UDNS with the number of spectral elements corresponding to a resolution of $N = 64$ and $N = 127$, respectively. The resolution of the reference SEM DNS corresponds to $N = 351$.

$\Theta = 10\Delta t$, $\chi = 2.0$, and $\Delta t = 0.005$. Below, both, underresolved DNS (denoted as UDNS) results and TLES computations, for SEM as well as LBM, are cross-compared with respect to the reference high resolution SEM DNS.

3.3.1. Underresolved direct numerical simulation

Fig. 7 summarizes dissipation rates, energy spectrum and dissipation spectrum for the TGV flow computed without turbulence model with LBM and SEM as UDNS for resolutions of $N = 64$ and $N \approx 128$, respectively.

Fig. 7a gathers the dissipation rates ϵ_{tot} , ϵ_{mod} and ϵ_{res} for LBM and ϵ_{tot} for SEM. The total dissipation rates in the initial region of both methods are similar for each resolution. However, the peak region is underpredicted by LBM in contrast to the SEM results. This effect is less pronounced for $N \approx 128$. For $N = 64$ the SEM seems to detect the dissipation rate peak better in terms of magnitude and narrowness around $t = 9$. Within the remaining time interval both methods show a certain variance from the DNS reference, where the LBM overpredicts and the SEM underpredicts the dissipation rate. For $N = 128$, the LBM approaches the peak magnitude of the dissipation rate and closely matches the slope in the time interval subsequent to the overpredicted plateau at $t \approx 13$. Similarly, the SEM closely follows the DNS roughly up to $t \approx 10$, and

deviates from the reference dissipation rate in the plateau region. However, the SEM also varies from the reference DNS in the final time interval by first underpredicting and then overpredicting the slope.

The qualities of each method for the recovery of the energy spectrum can be observed in Fig. 7b. Within the low wavenumber region, the SEM produces more accurate results than the LBM. This difference vanishes when increasing the resolution. In the high wavenumber region for $N = 64$ SEM produces an energy pile-up, whereas LBM predicts an early onset of the dissipation range with low energy levels. Increasing the resolution to $N \approx 128$ the SEM bends the pile-up towards the DNS which substantially increases the approximation quality. The energy spectrum recovered by the LBM still exhibits an early decay though its onset is shifted from $\kappa \approx 20$ (for $N = 64$) to $\kappa \approx 50$ (for $N = 128$).

For the dissipation spectra plotted in Fig. 7c similar effects are visible. The characteristic differences between the methods in terms of pile-up with SEM versus early energy dissipation with LBM are clearly apparent for $N = 64$. The increased resolution $N \approx 128$ still exhibits a separation of curves at higher wavenumbers. Up to $\kappa \approx 40$ both methods closely follow the DNS reference, where LBM slightly overpredicts the DNS dissipation spectrum for $\kappa \gtrsim 25$. Afterwards, the SEM dissipation spectrum still roughly matches the reference slope with a diminished pile-up at the highest captured wavenumbers, whereas the LBM triggers an early onset of flattening.

Overall, both, LBM and SEM, recover the tested quantities remarkably well in comparison to results with other methods but similar resolutions found in the literature [38,32]. Distinct attributes can be observed which root in the derivation of each method and leave scope for specific improvements or additional features.

3.3.2. Temporal large eddy simulation

Fig. 8 summarizes dissipation rates, energy spectrum and dissipation spectrum for the TGV flow computed with TLES with LBM and SEM for resolutions of $N = 64$ and $N \approx 128$, respectively.

With respect to the dissipation rates plotted in Fig. 8a, the LBM TLES recovers the formation of a distinct peak around $t \approx 9$ already at a resolution of $N = 64$, although with slightly differing magnitude. In contrast to that, the SEM exhibits a distorted crown within the peak region. As expected, initial time oscillations are clearly visible for LBM. The SEM shows similar but far less pronounced issues. The dissipation rate tail is overpredicted by the LBM and slightly underpredicted by the SEM. Increasing the resolution to $N \approx 128$, both methods closely follow the DNS reference up to $t \approx 9$. Afterwards, the LBM fails in capturing the plateau subsequent to the peak region, but aligns again with the reference slope for $t \gtrsim 13$. The SEM overpredicts and then underpredicts the DNS reference within this region.

Comparing the energy spectra in Fig. 8b for $N = 64$, the distinct features of each method reappear, i.e. the SEM forms an energy pile-up at high wave-numbers, whereas the LBM induces an early energy dissipation in that region. Again, these effects shift and decrease with an increased resolution of $N \approx 128$.

The dissipation spectra produced with TLES (see Fig. 8c) also exhibit similar properties as for UDNS. Nevertheless, a trend towards a closer match of the DNS reference is visible. The dissipation pile-up of SEM TLES is less distinctive compared to SEM UDNS. Analogously, the LBM TLES flattening is slightly shifted upwards compared to the LBM UDNS.

Overall, the most prominent differences between LBM TLES and LBM UDNS can be observed in the dissipation rates. Comparing UDNS and TLES results of LBM for $N = 64$ (Fig. 7a vs Fig. 8a, left respectively), we notice a sharpening effect of ϵ_{tot} in the peak region towards the DNS reference. This observation can be linked to ϵ_{mod} , which forms a peak closer to the reference peak at $t \approx 9$ with TLES than with UDNS. At the same time, the resolved dissipation rate ϵ_{res} appears to be smoother for LBM TLES than for LBM UDNS. Similarly, the SEM TLES results show better agreement with the DNS values for ϵ_{tot} than the SEM UDNS data.

Hence, for both methods, the TLES evidently improves the dissipation rate recovery, while upholding or slightly enhancing the good approximation of DNS reference energy and dissipation spectra. This improvement can be traced back to the injection of model dissipation rate.

After comparing the MRT LBM results of UDNS and TLES, we can make the conjecture that the employed MRT LBM UDNS, already acts as an implicit LES *on its own*. The model dissipation rate for $N = 64$ in Fig. 7a which makes approximately half of ϵ_{tot} underpins this remarkable feature.

3.4. Numerical error quantification

The mesh convergence of UDNS with MRT LBM for the TGV flow under acoustic scaling (AS) up to a measurable compressibility error has been investigated by Haussmann et al. [24]. Following up the work, the present investigations predict the accuracy of MRT LBM with the proposed TLES and link the activity of the model to an error extracted from the energy spectrum. The results of the explorative numerical experiments are gathered in Fig. 9.

Besides the classical evaluation of a turbulence model based on non-analytic graphical observations, a possible tool for measuring its accuracy is suggested by Geurts et al. [27]. The accuracy prediction is based on the subgrid activity

$$s(N, t) = \frac{\left| \epsilon_{\text{mod}}^{(N)}(t) \right|}{\left| \epsilon_{\text{tot}}^{(N)}(t) \right|}, \quad (29)$$

where $\epsilon^{(N)}(t)$ denotes the respective dissipation rate portions for a resolution N at time t . Note that we reframe the notions introduced in [27] specifically for the classical Smagorinsky model according to the observations for the present

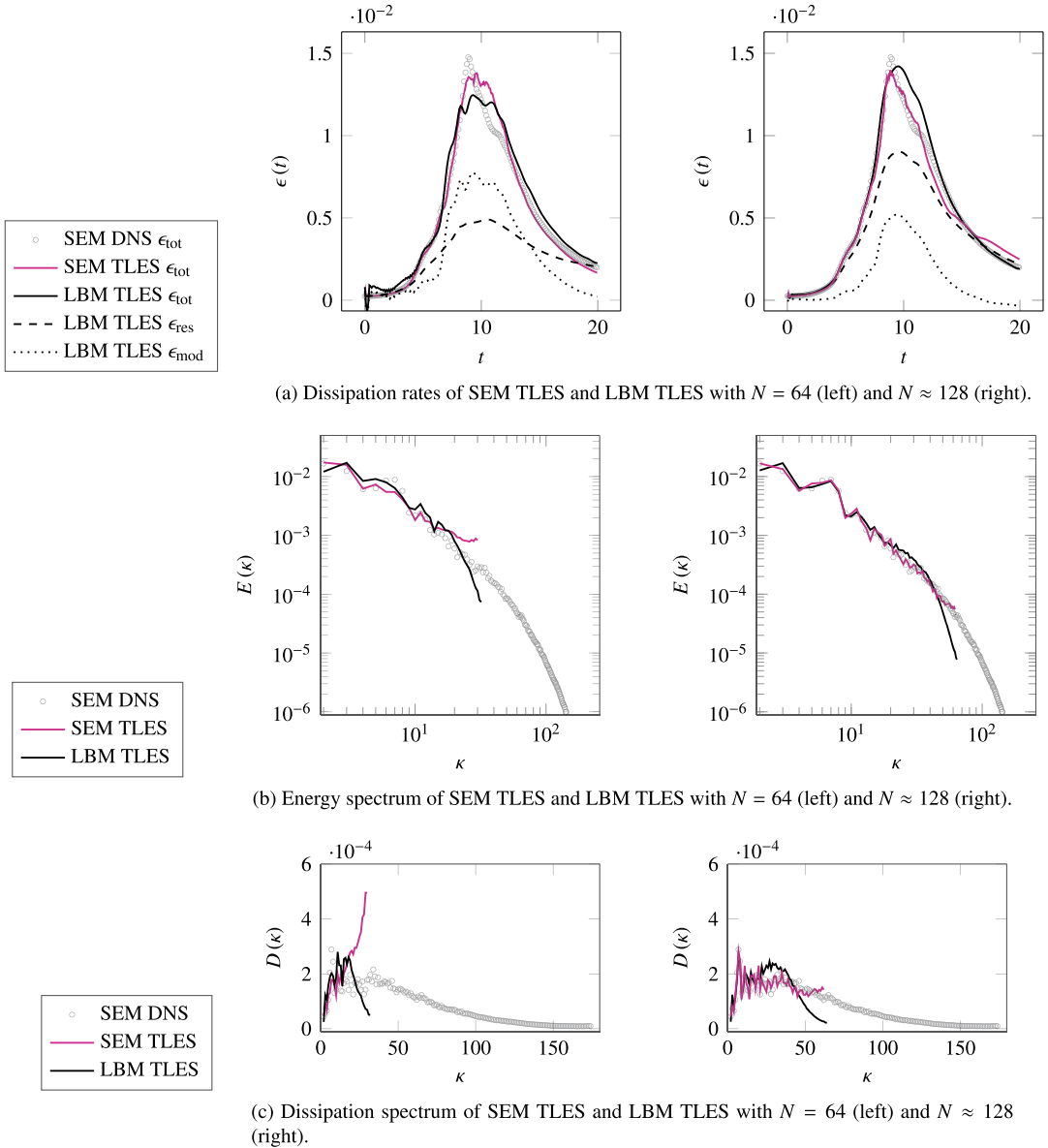


Fig. 8. Dissipation rates $\epsilon_{\text{tot}}(t)$, $\epsilon_{\text{res}}(t)$, $\epsilon_{\text{mod}}(t)$, energy spectrum $E(\kappa)$ (at $t = 9$) and dissipation spectrum $D(\kappa)$ for the TGV flow with $Re = 3000$. Computations for $N = 64$ (left column) and $N = 128$ (right column) with LBM TLES ($\tilde{\Theta} = 10$) for $Ma = 0.1$ compared to SEM TLES with the number of spectral elements corresponding to a resolution of $N = 64$ and $N = 127$, respectively. The resolution of the reference SEM DNS corresponds to $N = 351$.

TDDM. Subsequently, the accuracy of a run with resolution N is compiled into a time dependent L^2 -error over the resolved wavenumbers κ with respect to the energy spectrum $E^{(N)}(\kappa, t)$, i.e.

$$\text{err}_{L^2}(N, t) = \sqrt{\frac{\sum_{i=2}^c |E^{(N)}(\kappa_i, t) - E^{\text{DNS}}(\kappa_i, t)|^2}{\sum_{i=2}^c |E^{\text{DNS}}(\kappa_i, t)|^2}}, \quad (30)$$

where $\kappa_c = \kappa_c(N)$ denotes the cut-off wavenumber for the respective resolution.

The subgrid activity $s(N, t)$ of the MRT LBM TLES and the MRT LBM UDNS are plotted over time t for a resolution sequence of $N = 24, 48, 64, 96, 128, 192$ in Fig. 9a and Fig. 9b, respectively. The specific data at time $t = 9$ is compiled in Fig. 9c. The parameters for the spatial refinement obey AS with a constant Mach number $Ma = 0.1$ and the filter width is chosen as $\tilde{\Theta} = 10$. Exemplary parameter settings for $N = 64$ and $N = 128$ are listed in Table 1. Apart from the artifacts discussed in Section 3.2.2 which are clearly visible in Figs. 9a, 9b—namely the initialization errors at the beginning of the simulated time interval and the negative model dissipation rate values at its end—the subgrid activity is monotonically

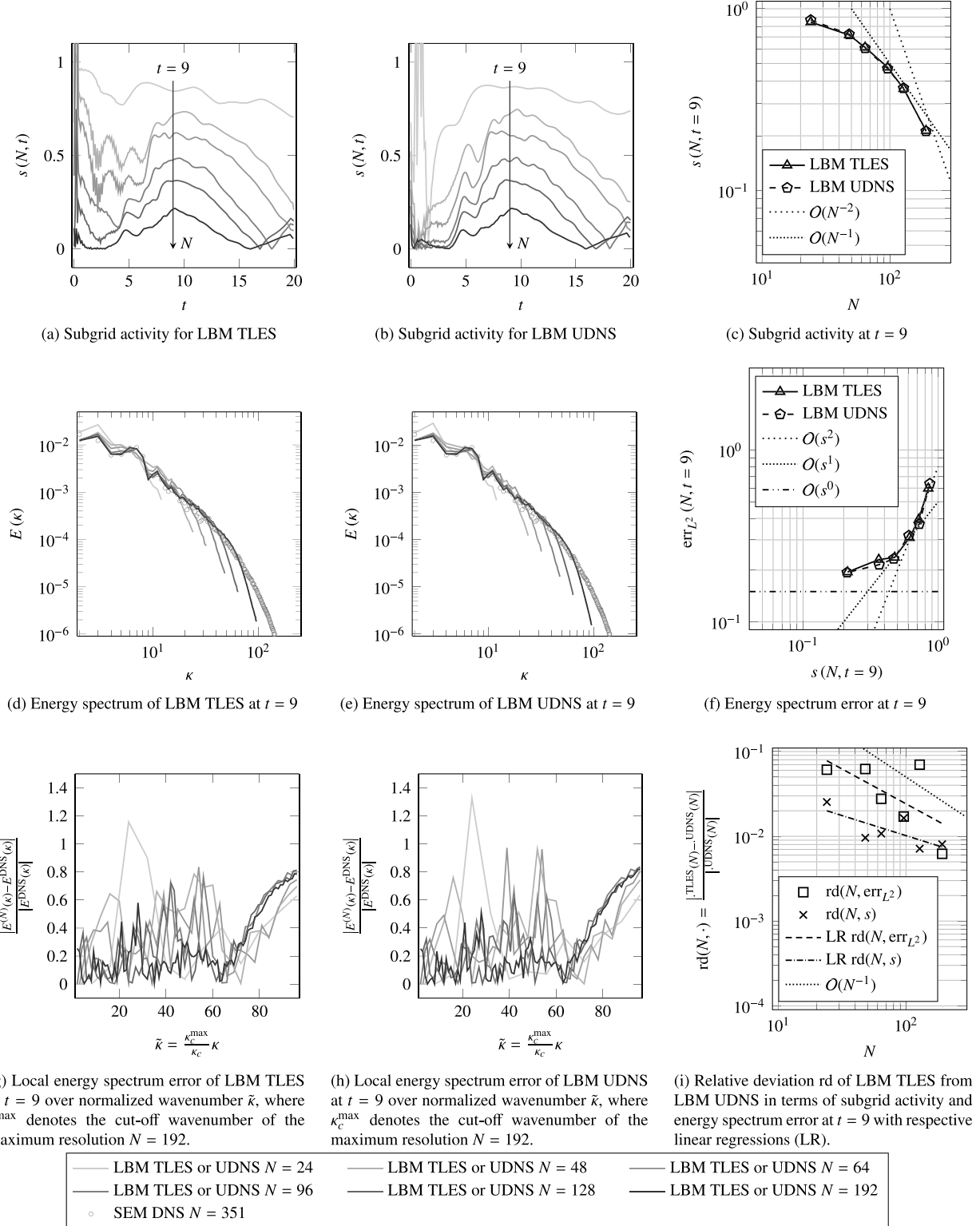


Fig. 9. Subgrid activity and energy spectrum error measurements for a sequence of resolutions $N = 24, 48, 64, 96, 128, 192$. LBM TLES with $\tilde{\Theta} = 10$ and LBM UDNS computations are carried out with $Ma = 0.1$ for the TGV flow at $Re = 3000$.

decreasing on average when the resolution is increased. This suggests a consistently vanishing subgrid contribution towards DNS level resolutions for the present TLES. Due to its time discretization dependence, the temporal filter width Θ is affected by increasing the temporal resolution along the spatial one during AS. The effect of this coupling is clearly visible in Fig. 9c.

It is notable that, when refining the grid via AS, the subgrid activity of *both* simulation techniques with MRT LBM is diminished with increasing (up to presumably second) order. Further, comparing Fig. 9a and Fig. 9b we observe solely shape differences within the artifact-free region $t \in (5, 15)$, whereas the general magnitude of the subgrid activity with and without explicit turbulence model remains approximately equal. Again, the above mentioned interpretation of MRT LBM as a stand-alone implicit turbulence model seems natural and is strongly supported by the data compiled in Fig. 9c.

To isolate the previously observed dissipation injection at the peak region of $\epsilon_{\text{tot}}(t)$, the energy spectra produced by the MRT LBM with and without TLES are evaluated at $t = 9$, see Fig. 9d and Fig. 9e, respectively. Within the dissipation regime for the highest wavenumbers, a slight increase of the slope produced by TLES compared to the UDNS result can be observed for all resolutions. The corresponding errors computed according to (30) are gathered in Fig. 9f by plotting $\text{err}_{L^2}(N, t = 9)$ over the subgrid activity $s(N, t = 9)$. For lower resolutions $N \leq 64$ an accuracy order of two is evident. Increasing the resolution, the second order accuracy in terms of $\text{err}_{L^2}(N)$ is diminished until an error plateau is reached.

Since the error plateau appears for both, UDNS and TLES, a further characterization is required. As a first investigation of isolating the impact of the TLES on LBM, Fig. 9i visualizes the relative deviation of the MRT LBM TLES from its UDNS counterpart in terms of subgrid activity and energy spectrum error. For both quantities, a clear diminishing trend is observable. Whereas the subgrid activity deviation shows a linear regression slope of approximately $\mathcal{O}(N^{-0.47})$, the regression slope of the energy spectrum error deviation exhibits a much clearer order $\mathcal{O}(N^{-0.83})$.

Further, the overall magnitude of the energy spectrum error plateau is almost doubled compared to the dissipation rate error values obtained in [24]. Figs. 9g, 9h gather additional information on the energy spectrum error composition in terms of normalized wavenumbers $\tilde{\kappa}$. Within the regime up to approximately 75% of the resolved wavenumbers, the error is on average consistently diminished with an increasing resolution. Opposed to that, the remaining 25% up to the cut-off wavenumber form an asymptotically constant error contribution and perturb the error measurement due to the dissipation rate tail. Hence, we expect that advanced analysis techniques (e.g. [39]) could be employed to focus on certain wavenumber ranges.

In summary, the information compressed in Figs. 9g, 9h, 9i suggests that the presence of numerical dissipation within the underlying method renders the experimental error analysis of the compound methodology, including the TLES, rather difficult. Nevertheless, we can state that, along the limit towards the error bound of MRT LBM with AS [24], the TLES consistently loses its model effectiveness represented by the subgrid activity. In terms of a *temporal subgrid resolution* defined as $\hbar = \Delta t / \Theta$, the present work proves that with $\hbar = 0.1$ being fixed as a constant, the solution to the incompressible NSE is approached by the proposed MRT LBM TLES up to a known combination of errors. Since the error plateau similarly appears for MRT LBM UDNS we conclude that, besides the dissipative nature of LBM, the compressibility defect [24] represents the main contribution of the energy spectrum error. A consistency error investigation with respect to the total dissipation rate is provided in Appendix B. However, the complete interaction of all possible roots of errors near the DNS level remains to be clarified in future studies.

4. Conclusion

An LBM TLES has been proposed via closure of the FDVBE [13] with the TDDM [20]. The suitability of the resulting numerical method has been evaluated for DHIT. A numerical calibration has been carried out via investigating the interplay of the lattice Mach number affecting the MRT LBM and the filter width which characterizes the TLES. We have isolated capabilities of the novel configuration of methods with respect to turbulence quantity recovery of highly resolved DNS results. Along the benchmark tests the present MRT LBM TLES has been compared to the recently proposed SEM TLES [20]. The TLES results for the herein considered TGV flow with both, SEM and MRT LBM are in qualitatively good agreement to the DNS reference data. For the MRT LBM TLES an error measurement with respect to the energy spectrum [27] has been conducted and linked to the subgrid activity. In addition, the consistency of the TDDM with first and second order finite difference discretization has been numerically confirmed via computing the total dissipation rate error for both SRT and MRT LBM, respectively.

In summary, the present work introduces and verifies the concept of employing a TDDM for LBM based on consistent filtering. We found that the proposed LBM TLES shows consistently enhanced dissipation rate recovery via model dissipation rate injection. At the same time, similar or slightly better results for energy and dissipation spectra are found with TLES compared to the data generated with UDNS. Further, it is notable that in contrast to the spatial ADM for LBM suggested by Malaspinas et al. [15], the present TLES with TDDM upholds the spatial locality of LBM. Hence we are able to exchange the computational load of the turbulence model with additional memory requirements for the usage of local data from previous timesteps. Aside from intrinsic numerical dissipation and compressibility defects, the subgrid activity determines the error of the method. Finally, we can conclude from the proposed accuracy prediction for TLES that under constant temporal subgrid resolution, the TLES subgrid activity vanishes when refining towards DNS level mesh sizes. Henceforth, the spatially valid concept of filtering is also approved for LBM TLES.

Nevertheless, small timesteps which keep down spurious oscillations within the initialization zone are necessary for LBM to operate near the incompressible regime. Thus, the diminishing of density fluctuations by consistent initialization

is required to validly apply the deconvolution model. Additionally, the Mach number dependency of the MRT remains crucial. Despite the fact that the MRT model used herein, carries optimized kinetic relaxation frequencies [23,22] and thus allows stable and for low to intermediate resolutions reasonably accurate computations, the collision operator still exhibits deficits. To uphold stability for coarse meshes and at the same time increase the accuracy of the method via reducing the numerical dissipation, advanced collision schemes [40] could be employed. In any case, the optimality features of the tunable relaxation frequencies should be refined via a redefinition specifically for the purpose of approximating filtered partial differential equations. Further, sophisticated tools for the accuracy evaluation of the LES should be used and refined to analyze in more details the above proclaimed interpretation of the MRT LBM as an implicit turbulence model. Also for the TLES, a complete subgrid activity interpretation with respect to time scales remains to be addressed.

The present study generates several routes for follow-up investigations. First, since we use an incompressibly derived turbulence model for a nearly incompressible method to approximate an incompressible TEQ, the development of a TLES for compressible NSE could be fruitful in regards of the weakly compressible nature of LBM. Alternatively, a density fluctuation suppression for LBM [41] with modified equilibria for truncation error correction [42] could enforce the incompressibility of LBM and ensure spatial isotropy for realistic scenarios with limited parameter spaces. Second, the construction of an LES in space and time to resemble the discretization along characteristics in the derivation of LBM might reveal improved consistency towards the TEQ. Third, the meaning of regularization for LBM should be observed from a completely different perspective as currently practiced. The TLES-typical regularization terms, which enable the bending of the SEM energy pile-up towards the DNS data [20], could be interpreted for LBM as artificial relaxation components [43] added to the moment system. Transferring these regularization terms to the LBM theory might lead to similarly positive effects for the LBM TLES. Hence, a theoretical analysis for isolating the effect of such additional terms on possible phase lag errors could yield promising insights. Fourth, the here used LBM TLES is designed as a numerical scheme based on computing observables which are governed by the time-filtered lattice Boltzmann equation. Reverting a possible phase lag under the premise of reasonable temporal resolution, the discretized temporal deconvolution thus recovers the initially sought for quantities in unfiltered state. The derivation of a bound for such reasonability should enhance the model parameter calibration drastically.

At last, it has to be stressed that isolating and subsequently outsourcing the overlaps of adjacent fields of research should be focused to produce a highly optimized turbulence model, which exhibits specialized features and reduced deficits with respect to the underlying numerical method. Such a combination of techniques remains of paramount interest, especially when considering hybrid methods which couple different approaches for the advanced simulation of turbulent flows at feasible computational effort.

CRediT authorship contribution statement

Stephan Simonis: Data curation, Formal analysis, Investigation, Methodology, Project administration, Software, Validation, Visualization, Writing – original draft, Writing – review & editing. **Daniel Oberle:** Data curation, Investigation, Methodology, Software, Validation, Visualization, Writing – review & editing. **Maximilian Gaedtke:** Conceptualization, Data curation, Investigation, Methodology, Software, Validation, Visualization, Writing – review & editing. **Patrick Jenny:** Resources, Supervision, Writing – review & editing. **Mathias J. Krause:** Funding acquisition, Resources, Software, Writing – review & editing.

Declaration of competing interest

The authors declare that they have no known competing financial interests or personal relationships that could have appeared to influence the work reported in this paper.

Acknowledgements

S.S. would like to thank Willy Dörfler for providing excellent supervision and the work facilities at the Institute for Applied and Numerical Mathematics at Karlsruhe Institute of Technology. This work is partially funded by DFG, KR4259.8-2, SPP 2045/1. Parts of this work were performed on the supercomputers ForHLR and HoreKa, both funded by the Ministry of Science, Research and the Arts Baden-Württemberg and by the Federal Ministry of Education and Research.

Appendix A. Methodological modifications

For the sake of completeness, we formulate and discuss modifications for the above presented methodological components. In Appendix B the resulting modular assemblies are then cross-compared in terms of numerical consistency along standard scaling laws for LBM.

A.1. Single-relaxation-time collision

In [24], several collision schemes are numerically evaluated in terms of experimental accuracy, consistency and stability for simulating the TGV flow. Therein, it is found that, despite being non-convergent for DS with static kinetic relaxation times, the MRT enhances the stability of LBM for underresolved DNS in comparison to SRT. Below, the correlation of this effect with the above formulated TLES is numerically investigated.

A.2. Model discretization with second order finite differences

As stated above, the here proposed method requires data from previous timesteps, which exchanges computational effort for memory storage capacity. Since the memory consumption thus directly correlates to the order of the model discretization, taking an accuracy trade-off into account seems reasonable. However, due to the standard LBM being generally regarded as second order in time and space, we investigate the impact of using a second order discretization also for the TDDM evolution rules (residual stress computation and deconvolution). A second order discretized TDDM is obtained by employing the two-step Adams–Bashforth method and injecting second order forward and central difference formulas for velocity derivatives at $t - 2\Delta t$ and $t - \Delta t$, respectively, which transforms (6) into

$$\begin{aligned} T_{\alpha\beta}(\mathbf{x}, t) = & \left(1 - \frac{3\Delta t}{2\Theta}\right) T_{\alpha\beta}(\mathbf{x}, t - \Delta t) + \frac{\Delta t}{2\Theta} T_{\alpha\beta}(\mathbf{x}, t - 2\Delta t) \\ & - \frac{\Theta}{2\Delta t} \left[\frac{1}{2} \bar{u}_\alpha(\mathbf{x}, t) - 2\bar{u}_\alpha(\mathbf{x}, t - \Delta t) + \frac{3}{2} \bar{u}_\alpha(\mathbf{x}, t - 2\Delta t) \right] \\ & \times \left[\frac{1}{2} \bar{u}_\beta(\mathbf{x}, t) - 2\bar{u}_\beta(\mathbf{x}, t - \Delta t) + \frac{3}{2} \bar{u}_\beta(\mathbf{x}, t - 2\Delta t) \right] \\ & + \frac{3\Theta}{8\Delta t} \left[\bar{u}_\alpha(\mathbf{x}, t) - \bar{u}_\alpha(\mathbf{x}, t - 2\Delta t) \right] \left[\bar{u}_\beta(\mathbf{x}, t) - \bar{u}_\beta(\mathbf{x}, t - 2\Delta t) \right]. \end{aligned} \quad (\text{A.1})$$

Backward differencing the deconvolution rule (5) with second order yields

$$\Upsilon(\mathbf{x}, t) = \bar{\Upsilon}(\mathbf{x}, t) + \frac{\Theta}{\Delta t} \left[\frac{3}{2} \bar{\Upsilon}(\mathbf{x}, t) - 2\bar{\Upsilon}(\mathbf{x}, t - \Delta t) + \frac{1}{2} \bar{\Upsilon}(\mathbf{x}, t - 2\Delta t) \right]. \quad (\text{A.2})$$

Equations (A.1) and (A.2) are used from $t = 2\Delta t$ onwards. Whereas for $t = 0$ the residual stress is nulled out by construction (since filtered and unfiltered fields coincide [20]), at time $t = \Delta t$ the approximations (A.1) and (A.2) can be replaced with (18) and (19), respectively. Note that locality in space is upheld.

Appendix B. Scaling, consistency and experimental order of convergence

Since we aim at approximating the incompressible NSE, DS is mathematically consistent in the relaxation limit and reduces the accuracy in time to first order ($\Delta t \sim \Delta x^2$) with respect to the TEQ (see [44–46]). In contrast to that, AS suggests spatio-temporal accuracy orders of two (since $\Delta t \sim \Delta x$), but prevents convergence as soon as the constant compressibility error plateau is reached (see theoretically [45] and numerically [24]). According to this fact, a second order TDDM discretization should be more consistent in underresolved configurations and AS. Whereas a first investigation of this conjecture is provided below, the detailed analysis is deferred to future studies. Moreover, despite AS being non-convergent, it is employed in the present study due to its common usage in underresolved applications with limited parameter spaces. Thus, the above investigations include numerical tests for the AS-typical error behavior which was previously documented in [24].

Nevertheless, from a mathematically rigorous point of view, the LBM as a numerical method to approximate the incompressible NSE is restricted to DS, which hence implies accuracy of second order in space and first order in time, and henceforth *in this case* renders the first order discretization of the TDDM (deconvolution and residual stress calculation) reasonable.

To investigate and verify these statements, the modular LBM combinations of SRT and MRT as UDNS and with TDDM finite difference discretization of first (TLES01) and second order (TLES02), respectively, are compared in terms of error measurements along AS and DS with respect to a Kolmogorov scale resolving high resolution simulation (SRT LBM with $N = 512$ and parameters according to Table 2). The validity of the highly resolved SRT LBM as DNS was numerically proven in [24] with respect to reference results obtained with pseudo-spectral methods. Note that, due to the observations made in [47], within the present work spatial velocity gradients are computed with eighth order central differences. Furthermore, (24) is approximated with second order central differences. The simulations are carried out on a maximum of 264 nodes with two Intel Xeon Platinum 8368 processors each.

Fig. 10 gathers the results of resolution dependent computations of the total dissipation rate error

$$\text{err}_{\epsilon_{\text{tot}}}(N) = \sqrt{\frac{\sum_{i=1}^m |\epsilon_{\text{tot}}^{(N)}(t_i) - \epsilon_{\text{tot}}^{\text{DNS}}(t_i)|^2}{\sum_{i=1}^m |\epsilon_{\text{tot}}^{\text{DNS}}(t_i)|^2}} \quad (\text{B.1})$$

for each tested modification, where $[t_1, t_m] = [0.1, 20]$ is discretized to equidistant time intervals of size 0.1, and $\epsilon_{\text{tot}}^{\text{DNS}}$ refers to the total dissipation rate computed with the high resolution SRT LBM. The corresponding discretization parameters are summarized in Table 1. Via linear regression, approximate EOC slopes are obtained from $\text{err}_{\epsilon_{\text{tot}}}(N)$ for the overall stable subsequence $N = 64, 128, 256$ (see Table 3).

Table 2
LBM discretization parameters used in Fig. 10.

N	scaling	Ma	τ	Δx	Δt
32	DS/AS	0.1	0.50106	0.20268	0.01170
	AS	0.1	0.50217	0.09973	0.00575
64	DS	0.05	0.50108	0.09973	0.00287
	AS	0.1	0.50437	0.04947	0.00285
128	DS	0.025	0.50109	0.04947	0.00071
	AS	0.1	0.50878	0.02463	0.00142
256	DS	0.0125	0.50109	0.02463	0.00017
	AS	0.00625	0.50110	0.01229	0.00004
512	DS				

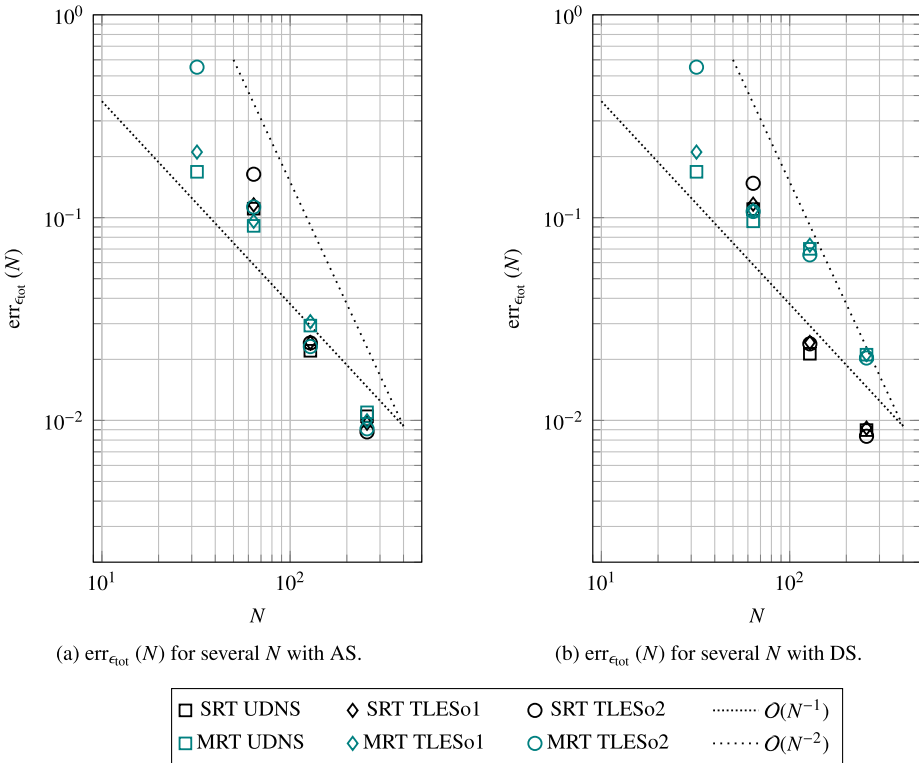


Fig. 10. EOC comparison for TGV flow computations at $Re = 800$ with modular LBM combinations of SRT or MRT without (UDNS) and with TLES with TDMM finite difference discretization of first (TLES01) and second order (TLES02), respectively. Only stable configurations are included. Total dissipation rate errors are calculated according to (B.1) with respect to high resolution reference data from SRT LBM at $N = 512$ and $Ma = 0.00625$. AS (left) and DS (right) are based on a respective sequence of resolutions $N = 32, 64, 128, 256$ starting at $Ma = 0.1$ and conforming to Table 2.

Table 3
Regression slopes $\mathcal{O}(N^{-\cdot})$ of EOC comparison (cf. Fig. 10) computed with $\text{err}_{\epsilon_{\text{tot}}} (N)$ for $N = 64, 128, 256$.

method	AS	DS
SRT UDNS	1.70	1.80
SRT TLES01	1.78	1.83
SRT TLES02	2.11	2.07
MRT UDNS	1.52	1.09
MRT TLES01	1.63	1.17
MRT TLES02	1.81	1.20

In advance of discussing Fig. 10 and Table 3, the statistical nature of EOC results for turbulent flow test cases without (known) analytical solution for all times has to be recalled. The rationale of this statement is based on several aspects, for example that the EOC computation via regression slopes is prone to interference by statistical outliers. Hence, in order to uphold a mathematical viewpoint, the perception of data obtained from such numerically experimental validations should remain rather fuzzy than accurate up to specific decimal places.

Nevertheless, considering the results compiled in Fig. 10, the following observations can be made. Firstly, comparing the SRT error results of the largest tested resolution $N = 256$ for AS and DS, we deduce that the compressibility error plateau is only marginally pronounced, which matches the observations in [24] where the DNS level for the present setting has been approximated to $N \approx 313$. This feature of the results proves the choice of an incompressible turbulence model for a weakly compressible method reasonable when using $Ma \leq 0.1$. Secondly, despite using MRT reduces the EOC (see Table 3), it yields a stability gain for highly underresolved settings (here $N = 32$) in comparison to BGK. Additionally, with the help of dynamic relaxation frequencies, the present MRT formulation is stable for all tested Mach numbers. Still, unexpectedly, the usage of MRT lowers the EOC in DS compared to AS by about 0.5 (see Table 3). This is not the case for SRT LBM. We interpret the effect as a consequence of choosing specific sets of relaxation frequencies which modify numerical dissipation, reduce the error for a fixed resolution, and thus yield crooked error curves. Moreover, the reduced EOC indicates that the present kinetic relaxation frequencies might be suboptimal with respect to a *filtered* TEQ. Thirdly, it has to be stressed that the TLES consistently improves the EOC in contrast to the UDNS for all tested methods and scalings. The positive impact of the model is larger for AS than for DS, which is likely due to the Ma reduction during DS. Further, the model effectiveness increases with the discretization order.

In summary it can be stated that, when using MRT with AS to ensure stability throughout a broad sequence of resolutions, the proposed concept of TLES for LBM significantly and consistently increases the EOC.

References

- [1] P. Lallemand, L.-S. Luo, M. Krafczyk, W.-A. Yong, The lattice Boltzmann method for nearly incompressible flows, *J. Comput. Phys.* 431 (2021) 109713, <https://doi.org/10.1016/j.jcp.2020.109713>.
- [2] C.K. Aidun, J.R. Clausen, Lattice-Boltzmann method for complex flows, *Annu. Rev. Fluid Mech.* 42 (1) (2010) 439–472, <https://doi.org/10.1146/annurev-fluid-121108-145519>.
- [3] L. Jahanshaloo, E. Pouryazdanpanah, N.A. Che Sidik, A review on the application of the lattice Boltzmann method for turbulent flow simulation, *Numer. Heat Transf., Part A, Appl.* 64 (11) (2013) 938–953, <https://doi.org/10.1080/10407782.2013.807690>.
- [4] A. Kajzer, J. Pozorski, K. Szewc, Large-eddy simulations of 3D Taylor-Green vortex: Comparison of smoothed particle hydrodynamics, lattice Boltzmann and finite volume methods, *J. Phys. Conf. Ser.* 530 (2014) 012019, <https://doi.org/10.1088/1742-6596/530/1/012019>.
- [5] M.F. Barad, J.G. Kocheemoolayil, C.C. Kiris, Lattice Boltzmann and Navier-Stokes Cartesian CFD approaches for airframe noise predictions, in: 23rd AIAA Computational Fluid Dynamics Conference, 2017, p. 4404, <https://doi.org/10.2514/6.2017-4404>.
- [6] M. Haussmann, F. Ries, J.B. Jeppener-Haltenhoff, Y. Li, M. Schmidt, C. Welch, L. Illmann, B. Böhm, H. Nirschl, M.J. Krause, A. Sadiki, Evaluation of a near-wall-modeled large eddy lattice Boltzmann method for the analysis of complex flows relevant to IC engines, *Computation* 8 (2) (2020) 43, <https://doi.org/10.3390/computation8020043>.
- [7] M.J. Krause, A. Kummerländer, S.J. Avis, H. Kusumaatmaja, D. Dapelo, F. Klemens, M. Gaedtke, N. Hafen, A. Mink, R. Trunk, J.E. Marquardt, M.-L. Maier, M. Haussmann, S. Simonis, OpenLB—open source lattice Boltzmann code, *Comput. Math. Appl.* 81 (2021) 258–288, <https://doi.org/10.1016/j.camwa.2020.04.033>.
- [8] R. Löhner, Towards overcoming the LES crisis, *Int. J. Comput. Fluid Dyn.* 33 (3) (2019) 87–97, <https://doi.org/10.1080/10618562.2019.1612052>.
- [9] S. Hou, J. Sterling, S. Chen, G.D. Doolen, A lattice Boltzmann subgrid model for high Reynolds number flows, <https://arxiv.org/abs/comp-gas/9401004>, 1994.
- [10] Y.-H. Dong, P. Sagaut, S. Marie, Inertial consistent subgrid model for large-eddy simulation based on the lattice Boltzmann method, *Phys. Fluids* 20 (3) (2008) 35104, <https://doi.org/10.1063/1.2842379>.
- [11] K.N. Premnath, M.J. Pattison, S. Banerjee, Dynamic subgrid scale modeling of turbulent flows using lattice-Boltzmann method, *Physica A* 388 (13) (2009) 2640–2658, <https://doi.org/10.1016/j.physa.2009.02.041>.
- [12] M. Weickert, G. Teike, O. Schmidt, M. Sommerfeld, Investigation of the LES WALE turbulence model within the lattice Boltzmann framework, *Comput. Math. Appl.* 59 (7) (2010) 2200–2214, <https://doi.org/10.1016/j.camwa.2009.08.060>.
- [13] O. Malaspina, P. Sagaut, Consistent subgrid scale modelling for lattice Boltzmann methods, *J. Fluid Mech.* 700 (2012) 514–542, <https://doi.org/10.1017/jfm.2012.155>.
- [14] P. Sagaut, Toward advanced subgrid models for lattice-Boltzmann-based large-eddy simulation: theoretical formulations, *Comput. Math. Appl.* 59 (7) (2010) 2194–2199, <https://doi.org/10.1016/j.camwa.2009.08.051>.
- [15] O. Malaspina, P. Sagaut, Advanced large-eddy simulation for lattice Boltzmann methods: the approximate deconvolution model, *Phys. Fluids* 23 (10) (2011), <https://doi.org/10.1063/1.3650422>.
- [16] S. Marié, X. Glerfelt, Adaptive filtering for the lattice Boltzmann method, *J. Comput. Phys.* 333 (2017) 212–226, <https://doi.org/10.1016/j.jcp.2016.12.017>.
- [17] P. Nathen, M. Haussmann, M.J. Krause, N.A. Adams, Adaptive filtering for the simulation of turbulent flows with lattice Boltzmann methods, *Comput. Fluids* 172 (2018) 510–523, <https://doi.org/10.1016/j.compfluid.2018.03.042>.
- [18] J. Jacob, O. Malaspina, P. Sagaut, A new hybrid recursive regularised Bhatnagar–Gross–Krook collision model for lattice Boltzmann method-based large eddy simulation, *J. Turbul.* 19 (11) (2018) 1051–1076, <https://doi.org/10.1080/14685248.2018.1540879>.
- [19] C. Pruett, Temporal large-eddy simulation: theory and implementation, *Theor. Comput. Fluid Dyn.* 22 (3–4) (2008) 275–304, <https://doi.org/10.1007/s00162-007-0063-0>.
- [20] D. Oberle, C.D. Pruett, P. Jenny, Temporal large-eddy simulation based on direct deconvolution, *Phys. Fluids* 32 (6) (2020) 065112, <https://doi.org/10.1063/5.0006637>.
- [21] D. d’Humière, Multiple-relaxation-time lattice Boltzmann models in three dimensions, *Philos. Trans. R. Soc. Lond. A, Math. Phys. Eng. Sci.* 360 (1792) (2002) 437–451, <https://doi.org/10.1098/rsta.2001.0955>.
- [22] S. Simonis, M. Haussmann, L. Kronberg, W. Dörfler, M.J. Krause, Linear and brute force stability of orthogonal moment multiple-relaxation-time lattice Boltzmann methods applied to homogeneous isotropic turbulence, *Philos. Trans. R. Soc. Lond. A, Math. Phys. Eng. Sci.* 379 (2208) (2021) 20200405, <https://doi.org/10.1098/rsta.2020.0405>.

- [23] M. Chávez-Modena, A. Martínez-Cava, G. Rubio, E. Ferrer, Optimizing free parameters in the D3Q19 multiple-relaxation lattice Boltzmann methods to simulate under-resolved turbulent flows, *J. Comput. Sci.* 45 (2020) 101170, <https://doi.org/10.1016/j.jocs.2020.101170>.
- [24] M. Haussmann, S. Simonis, H. Nirschl, M.J. Krause, Direct numerical simulation of decaying homogeneous isotropic turbulence—numerical experiments on stability, consistency and accuracy of distinct lattice Boltzmann methods, *Int. J. Mod. Phys. C* 30 (09) (2019) 1950074, <https://doi.org/10.1142/S0129183119500748>.
- [25] M. Krause, S. Avis, H. Kusumaatmaja, D. Dapelo, M. Gaedtke, N. Hafen, M. Haußmann, J. Jeppener-Haltenhoff, L. Kronberg, A. Kummerländer, J. Marquardt, T. Pertzel, S. Simonis, R. Trunk, M. Wu, A. Zarth, OpenLB Release 1.4: Open Source Lattice Boltzmann Code (Nov. 2020), <https://doi.org/10.5281/zenodo.4279263>.
- [26] Argonne National Laboratory, <https://nek5000.mcs.anl.gov>, 2019.
- [27] B.J. Geurts, J. Fröhlich, A framework for predicting accuracy limitations in large-eddy simulation, *Phys. Fluids* 14 (6) (2002) L41–L44, <https://doi.org/10.1063/1.1480830>.
- [28] P.J. Dellar, Bulk and shear viscosities in lattice Boltzmann equations, *Phys. Rev. E* 64 (3) (2001) 031203, <https://doi.org/10.1103/PhysRevE.64.031203>.
- [29] M.E. Brachet, Direct simulation of three-dimensional turbulence in the Taylor–Green vortex, *Fluid Dyn. Res.* 8 (1–4) (1991) 1–8, [https://doi.org/10.1016/0169-5983\(91\)90026-F](https://doi.org/10.1016/0169-5983(91)90026-F).
- [30] A. Krämer, D. Wilde, K. Küllmer, D. Reith, H. Foysi, Pseudoentropic derivation of the regularized lattice Boltzmann method, *Phys. Rev. E* 100 (2) (2019) 023302, <https://doi.org/10.1103/PhysRevE.100.023302>.
- [31] J. DeBonis, Solutions of the Taylor–Green vortex problem using high-resolution explicit finite difference methods, in: 51st AIAA Aerospace Sciences Meeting Including the New Horizons Forum and Aerospace Exposition, 2013, p. 382.
- [32] D. Fauconnier, C. Bogey, E. Dick, On the performance of relaxation filtering for large-eddy simulation, *J. Turbul.* 14 (1) (2013) 22–49, <https://doi.org/10.1080/14685248.2012.740567>.
- [33] S.B. Pope, *Turbulent Flows*, Cambridge University Press, 2001.
- [34] M. Wilczek, Y. Narita, Wave-number-frequency spectrum for turbulence from a random sweeping hypothesis with mean flow, *Phys. Rev. E* 86 (6) (2012) 066308, <https://doi.org/10.1103/PhysRevE.86.066308>.
- [35] M.O. Deville, P.F. Fischer, E.H. Mund, *High-Order Methods for Incompressible Fluid Flow*, vol. 9, Cambridge University Press, 2002.
- [36] P.J. Dellar, Incompressible limits of lattice Boltzmann equations using multiple relaxation times, *J. Comput. Phys.* 190 (2003) 351–370, [https://doi.org/10.1016/S0021-9991\(03\)00279-1](https://doi.org/10.1016/S0021-9991(03)00279-1).
- [37] R. Mei, L.-S. Luo, P. Lallemand, D. d'Humières, Consistent initial conditions for lattice Boltzmann simulations, *Comput. Fluids* 35 (8–9) (2006) 855–862, <https://doi.org/10.1016/j.compfluid.2005.08.008>.
- [38] L. Fu, X.Y. Hu, N.A. Adams, A new class of adaptive high-order targeted ENO schemes for hyperbolic conservation laws, *J. Comput. Phys.* 374 (2018) 724–751, <https://doi.org/10.1016/j.jcp.2018.07.043>.
- [39] B.J. Geurts, Analysis of errors occurring in large eddy simulation, *Philos. Trans. R. Soc. Lond. A, Math. Phys. Eng. Sci.* 367 (1899) (2009) 2873–2883, <https://doi.org/10.1098/rsta.2009.0001>.
- [40] C. Coreixas, B. Chopard, J. Latt, Comprehensive comparison of collision models in the lattice Boltzmann framework: theoretical investigations, *Phys. Rev. E* 100 (2019) 033305, <https://doi.org/10.1103/PhysRevE.100.033305>.
- [41] X. He, L.-S. Luo, Lattice Boltzmann model for the incompressible Navier–Stokes equation, *J. Stat. Phys.* 88 (3) (1997) 927–944, <https://doi.org/10.1023/B:JOSS.0000015179.12689.e4>.
- [42] M. Bauer, G. Silva, U. Rüde, Truncation errors of the D3Q19 lattice model for the lattice Boltzmann method, *J. Comput. Phys.* 405 (2020) 109111, <https://doi.org/10.1016/j.jcp.2019.109111>.
- [43] S. Simonis, M. Frank, M.J. Krause, On relaxation systems and their relation to discrete velocity Boltzmann models for scalar advection–diffusion equations, *Philos. Trans. R. Soc. Lond. A, Math. Phys. Eng. Sci.* 378 (2175) (2020) 20190400, <https://doi.org/10.1098/rsta.2019.0400>.
- [44] S. Uberbittini, P. Asinari, S. Succi, Three ways to lattice Boltzmann: a unified time-marching picture, *Phys. Rev. E* 81 (2010) 016311, <https://doi.org/10.1103/PhysRevE.81.016311>.
- [45] D.J. Holdych, D.R. Noble, J.G. Georgiadis, R.O. Buckius, Truncation error analysis of lattice Boltzmann methods, *J. Comput. Phys.* 193 (2) (2004) 595–619, <https://doi.org/10.1016/j.jcp.2003.08.012>.
- [46] M. Junk, A. Klar, L.-S. Luo, Asymptotic analysis of the lattice Boltzmann equation, *J. Comput. Phys.* 210 (2) (2005) 676–704, <https://doi.org/10.1016/j.jcp.2005.05.003>.
- [47] M. Geier, S. Lenz, M. Schönherr, M. Krafczyk, Under-resolved and large eddy simulations of a decaying Taylor–Green vortex with the cumulant lattice Boltzmann method, *Theor. Comput. Fluid Dyn.* 35 (2) (2021) 169–208, <https://doi.org/10.1007/s00162-020-00555-7>.